Estabrook, C. H., Weber, M., Kind, R. (1997): Generation of the teleseismic P-wave coda from Aleutian earthquakes. - Geophysical Journal International, 130, 2, pp. 349—364.

DOI: https://doi.org/10.1111/j.1365-246X.1997.tb05652.x

*Geophys. J. Int.* (1997) **130**, 349–364

# Generation of the teleseismic *P*-wave coda from Aleutian earthquakes

Charles H. Estabrook,[1] Michael Weber[2] and Rainer Kind[1]

[1] *GeoForschungsZentrum-Potsdam, Telegrafenberg, 14473 Potsdam, Germany. E-mail: chuck@gfz-potsdam.de*
[2] *Institut für Geophysik, Universität Göttingen, 37075 Göttingen, Germany*

Accepted 1997 March 20. Received 1997 March 18; in original form 1996 October 24

## SUMMARY

We investigate large-amplitude phases arriving in the *P*-wave coda of broad-band seismograms from teleseisms recorded by the Gräfenberg array, the German Regional Seismic Network and the Global Seismic Network. The data set consists of all events $m_b \geq 5.6$ from the Aleutian arc between 1977 and 1992. Earthquakes with large-amplitude coda waves correlate with the presence of oceanic crust in the source region. The amplitudes sometimes approach those of the *P* wave, much larger than predicted by theory. Modelling indicates that phases in the *P*-wave coda cannot be *P*-wave multiples beneath the source and receiver, or underside reflections, which precede *PP*, from upper-mantle discontinuities. Among the events, seismograms are very similar, where the arrival times of the unusual phases agree approximately with the predicted times of *S*-to-*P* conversions from the upper-mantle discontinuities under the source. Because the large-amplitude phases in the *P*-wave coda have little, if any, dependence on event depth and have predominantly an *SV*-wave radiation pattern towards the receiver, we suggest that they originate as *SV* and/or Rayleigh waves and are enhanced by lateral heterogeneity and multipathing from the subducting Aleutian slab.

**Key words:** Aleutian Islands, crust, seismic coda, seismic-wave propagation, subduction.

## INTRODUCTION

The *P*-wave coda, the interval between the initial *P* wave and the *PP* wave (a *P* wave reflected at the free surface midway between the source and the receiver), contains abundant information about Earth structure. The coda waves are caused through processes of conversion (e.g. *S* wave to *P* wave), reflection and scattering. However, central to studies of the coda are the degree of determinism involved in the conversions and reflections of the primary energy. We will address this point using broad-band seismograms from earthquakes in the Aleutian Islands recorded by the German and global seismic networks.

At local and regional distances and at high frequencies, *P* coda waves are thought to be generated through a stochastic process of single or multiple scattering of the primary *P* wave (e.g. Aki & Chouet 1975; Sato 1994), *P*-to-*P* and *P*-to-*SV* scattering from irregular interfaces (e.g. Dainty & Schultz 1995), and near-source isotropic scatterers (e.g. Lay 1987; Lynnes & Lay 1989). The teleseismic coda (at lower frequencies) has been attributed to reflections and conversions in the vicinity of the source and receiver, and to a minor extent to reflections from the region of the *PP* bounce point (e.g. Ward 1978; Shearer 1991). In Fig. 1, a plot of seismograms for the interval from the *P* wave to the *PP* wave calculated with the reflectivity method (Kind 1979) shows that a radial earth model predicts this interval to be composed of waves of source- and receiver-side *P* multiples, *S*-to-*P* conversions, and underside reflections from upper-mantle discontinuities (Shearer 1991; Estabrook & Kind 1996). The coda is generally of small amplitude and typically less than 10 per cent of the *P* wave (Fig. 1a), but for a focal mechanism which favours *SV* radiation, coda amplitudes can approach 25 per cent of *P* (Fig. 1b).

Previous investigators (e.g. Bolt, O'Neill & Qamar 1968; Wright & Muirhead 1969; Wright 1972; Cleary, King & Haddon 1975; King, Haddon & Husebye 1975) suggested that precursors to *PP* (also in the coda of the *P* wave) are caused by random reflections from the bounce point, since *PP* is a minimax phase (Aki & Richards 1980, pp. 410–411). Neele & Snieder (1991), from an analysis of data from the Gräfenberg (GRF) and NARS arrays, observed that the long-period *P* coda (5–50 s period) was coherent (over a 10 km station spacing), arrived along a great-circle path and concluded that it does not contain a significant amount of scattered energy. For the later phases, *PP*, *PPP* and *S*, Neele & Snieder (1991) observed that the codas are incoherent and suggest that this is caused almost entirely by body-to-surface-wave scattering

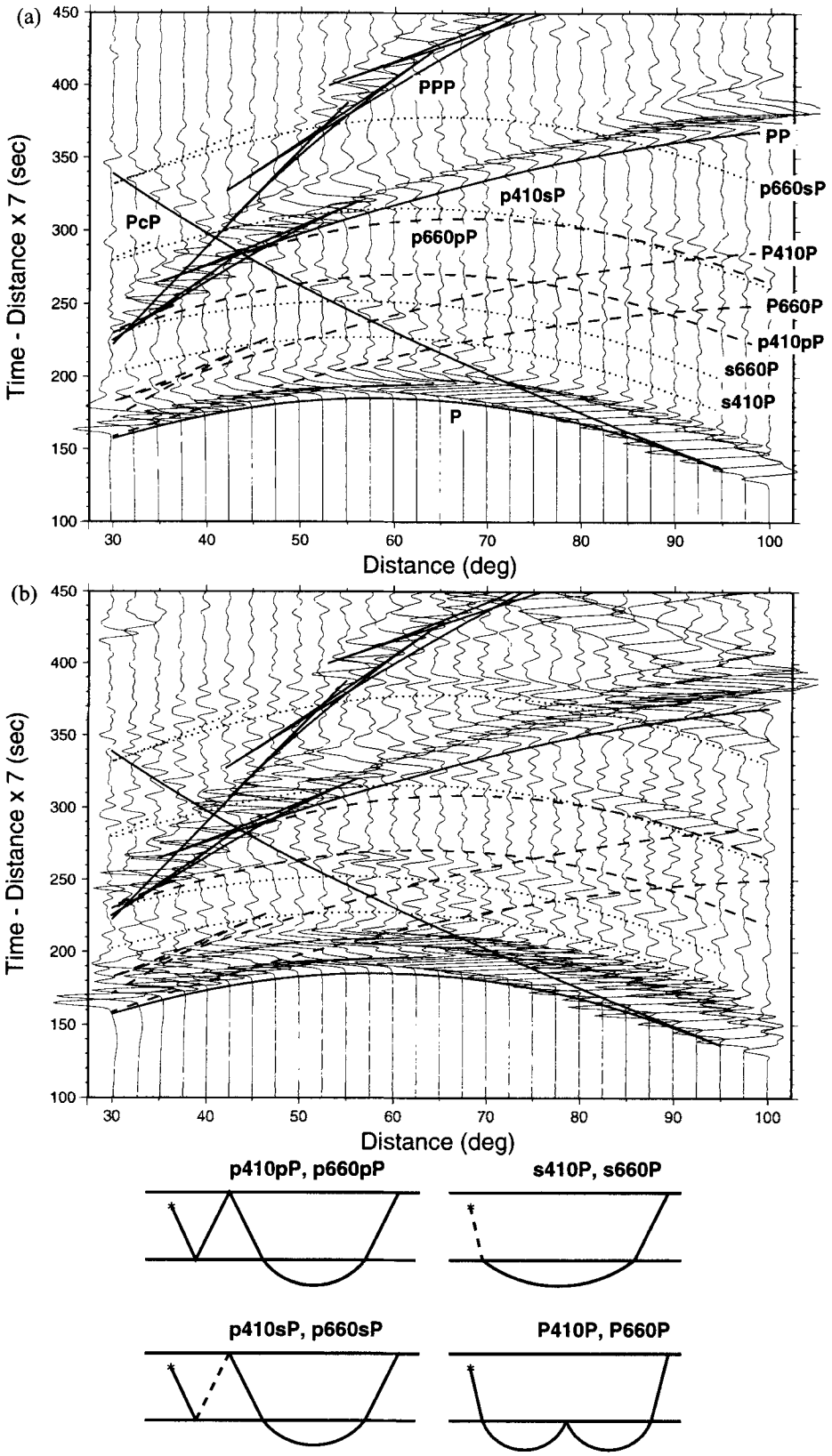


**Figure 1.** Synthetic seismograms calculated with the reflectivity method (Kind 1979) for the distance range 30°–100° showing phases in the *P*-wave coda. Vertical seismograms are plotted with a reduction slowness of 7 s/° and are normalized to the maximum trace amplitude. Lines are predicted arrival times from the IASP91 model (Kennett & Engdahl 1991) for a source at 5 km depth. Solid lines are the main phases, dotted lines are *S*-to-*P* conversions, and dashed lines are multiples and reflections from the discontinuities. Parameters and model are the same in (a) and (b) except for differing focal mechanisms: the mechanism in (a) radiates substantial *P* energy at this azimuth while that in (b) radiates more *SV* energy. The maximum amplitude in (a) is about 10 times larger than in (b). Shown at the bottom are sketches of the dominant upper-mantle phases.

and is more subject to multipathing from 3-D structure than are the earlier phases.

*S*-to-*P* conversions from upper-mantle discontinuities, which have their conversion points beneath the recording stations, are relatively easy to observe on long-period seismograms as precursors to *S* (Faber & Müller 1980; Bock & Kind 1991). On the other hand, *S*-to-*P* conversions originating in the upper mantle near the source and arriving shortly after the *P* wave are much more difficult to identify, and so far only a few observations have been made, mainly on short-period seismograms of deep earthquakes (Barley, Hudson & Douglas 1982; Bock & Ha 1984; Richards & Wicks 1990; Wicks & Richards 1991; Vidale & Benz 1992; Ritsema, Hagerty & Lay 1995). Kind & Seidl (1982, 1984, 1986) and Estabrook, Bock & Kind (1994) suggested that anomalously strong phases in teleseismic broad-band seismograms between the *P* wave and depth phases are *S*-to-*P* converted phases under the earthquake source. Precursors to *ScS* (*S*-to-*P*) have been used to map the subducting slab–mantle boundary under Japan (e.g. Nakanishi 1980; Hori *et al.* 1985; Helffrich & Stein 1993). Weber & Wicks (1996) and Wicks *et al.* (1997) demonstrated that with seismic broad-band arrays it is possible to detect and analyse phases in the teleseismic *P*-wave coda that are produced by heterogeneities near the source.

In this paper, we analyse the teleseismic *P*-wave coda of Aleutian earthquakes using broad-band array data from the German and global networks and suggest that large-amplitude phases originate as *SV* waves which are converted to *P* waves from laterally heterogeneous structure and from upper-mantle discontinuities in the source region.

## DATA AND OBSERVATIONS

The data set consists of seismograms from 164 Alaskan and Aleutian earthquakes that occurred between 1977 and 1992 and were recorded by the GRF array. The GRF array in Bavaria, Germany (Harjes & Seidl 1978), consists of 13 broad-band vertical stations (flat to velocity from 5 Hz to 20 s) and three three-component stations, and has a N–S aperture of about 100 km. The data set is supplemented with seismograms from the German Regional Seismic Network (GRSN) and the Global Seismic Network (GSN). The events have magnitudes larger than 5.6 $m_b$, depths less than 80 km, and are 65° to 80° epicentral distance from the German arrays. Some of the data were analysed using methods from Stammler (1992, 1993). Unless otherwise noted, *P*-wave beams, calculated from seismograms from the vertical GRF stations, are used in the analysis. Fig. 2 shows the distribution of events along the Aleutian arc.

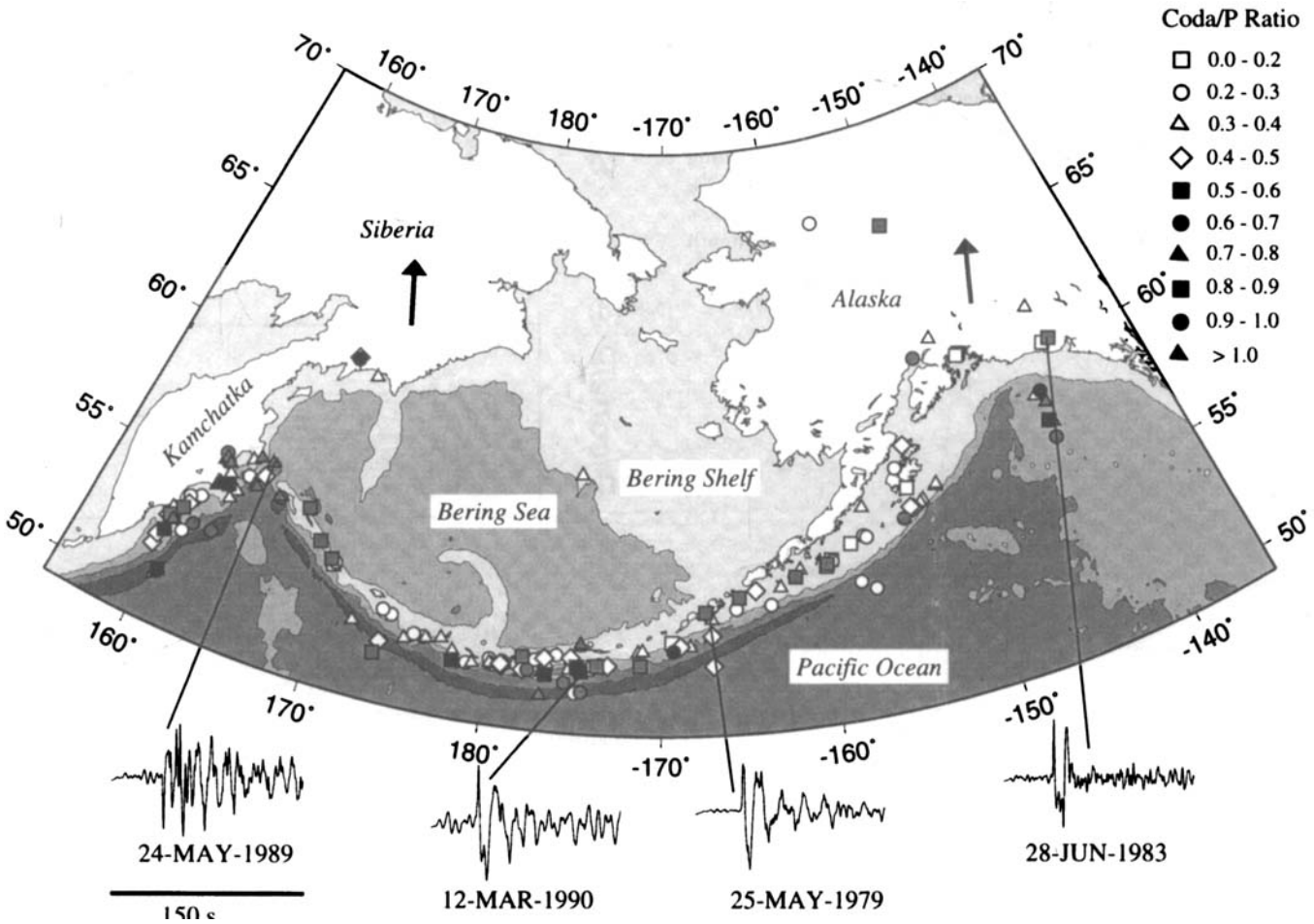


**Figure 2.** Map showing the epicentral distribution of the 164 events used in this study. Event locations are from the preliminary determination of epicentres (PDE). Events are graded by the peak-to-peak amplitude ratio of the coda to the *P* wave. Vertical broad-band velocity seismograms from station GRA1 are shown as examples from along the Aleutian arc. Bathymetry is contoured every 2 km starting at 1 km depth. Arrows indicate the direction to the German arrays, relative to map north.

Events under Alaska (e.g. 28-JUN-1983) are characterized by impulsive *P* waves with a low-amplitude coda. Eastern Aleutian events (e.g. 25-MAY-1979) have high-amplitude *P* waves with nearly monochromatic codas. Central Aleutian events (e.g. 12-MAR-1990) have impulsive *P* waves and high-amplitude codas. Western Aleutian events (e.g. 24-MAY-1989) often have *P*-wave codas of amplitudes approaching that of the *P* wave.

A typical seismogram of an event in the eastern Aleutians is given in Fig. 3. To demonstrate the frequency dependence of phases in the *P*-wave coda, we filter the seismogram to simulate seismometers of varying frequency bands. Broad-band velocity and the WWSSN-SP show little evidence of phases in the *P*-wave coda, while broad-band displacement, WWSSN-LP and SRO-LP show a large coda phase (phase X) at about 60 s after the *P* wave. Because X has the largest coda amplitude in the WWSSN-LP trace (about 40 per cent of the *P* wave) we will use this filter in the analysis of the GRF data.

To quantify seismic energy in the *P*-wave coda, we determine the coda-to-*P*-wave amplitude ratio for the entire data set (Fig. 4). The data set used here consists of *P*-wave beams of the vertical GRF seismograms from the 164 events (Fig. 2), filtered with the WWSSN-LP simulation filter. We define the '*P*-wave signal' as having 40 s duration. It includes the direct *P* wave and the depth phases (*pP* and *sP*). The maximum 'coda' amplitude is measured between 40 and 140 s after the *P*-wave onset. The chosen time-interval ends just prior to *PP*. *PcP* occurs in this time-window at distances shorter than 65°, but it is easily identified by its distance moveout (smaller slowness than the *P* wave) and therefore should not appear in the *P*-wave beamed seismograms. In Fig. 4(a) the coda/signal ratio (*P* coda/*P*) is plotted as a function of longitude along the Aleutian arc. For all events, the values range from 0.14–1.14, with an average of $0.44 \pm 0.21$ ($1\sigma$). Analysis of the data shows that the coda/*P* amplitude ratios do not depend on focal depth for events shallower than 80 km. The values of the observed

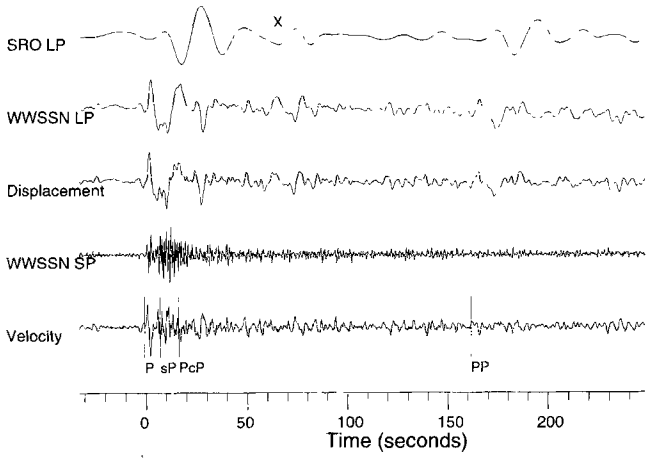


**Figure 3.** Application of different filters to simulate seismometers of varying frequency bands for a vertical seismogram at the station GRA1 from the event 6-SEP-1982 in the eastern Aleutians: location (56.87°N, 151.53°W), depth 19 km, 5.7 $m_b$, epicentral distance 72.8°. 'Velocity' is unfiltered broad-band velocity; 'WWSSN SP' and 'WWSSN LP' are short-period and long-period WorldWide Standard Seismic Network simulations; 'Displacement' has the instrument response deconvolved; 'SRO LP' is the long-period Seismic Research Observatory simulation. Predicted arrival times are from the IASP91 model. 'X' marks the arrival of the large-amplitude phase in the coda.

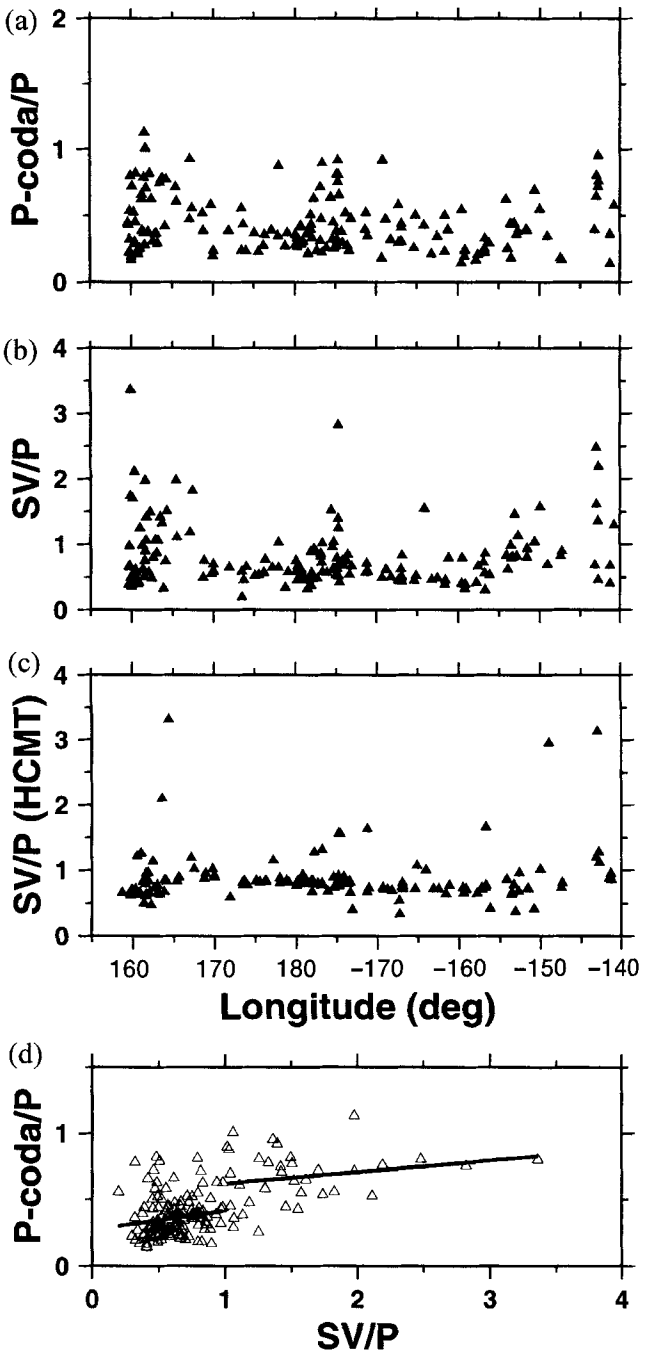


**Figure 4.** (a) Observed *P*-coda/*P*-wave amplitude ratio plotted as a function of longitude for GRF seismograms from events in Fig. 2. (b) Observed *SV*/*P* ratio for the events plotted in Fig. 2. *SV*-wave amplitude is the maximum peak-to-peak value from 5 s before the predicted *S* arrival time to 60 s after. *SV* measurements are taken from the beam of the N–S component of the stations GRA1, GRB1 and GRC1 since the backazimuth to the Aleutians is about 0°N. (c) Theoretical *SV*/*P* ratios calculated using Harvard CMT focal mechanisms and depths to station GRA1. (d) Observed *P*-coda/*P*-wave amplitude ratio from (a), plotted against observed *SV*/*P* ratio from (b), showing a linear relationship between the amplitude of the *P* coda and the *SV* wave. Solid lines are the best-fit lines (in a least-squares sense) to the data for $SV/P \leq 1$ and $SV/P > 1$. See text for details.

coda amplitudes are much larger than predicted by synthetic seismograms for a radially symmetric earth model (5–25 per cent).

A change from lower to higher coda amplitudes occurs near 170°W along the Aleutian arc (Figs 2 and 4). West of this point, in the central Aleutians, coda amplitudes tend to have larger values. This is near where the overriding plate changes from continental to oceanic (e.g. Davies *et al.* 1981; Klemperer *et al.* 1995). A bend or tear in the downgoing Pacific plate (e.g. Jacob, Nakamura & Davies 1977) with an accompanying change in dip of the subducting Pacific plate (Taber, Billington & Engdahl 1991) and seismic stress orientation (e.g. Estabrook & Jacob 1991; Lu & Wyss 1996), also occurs in this region.

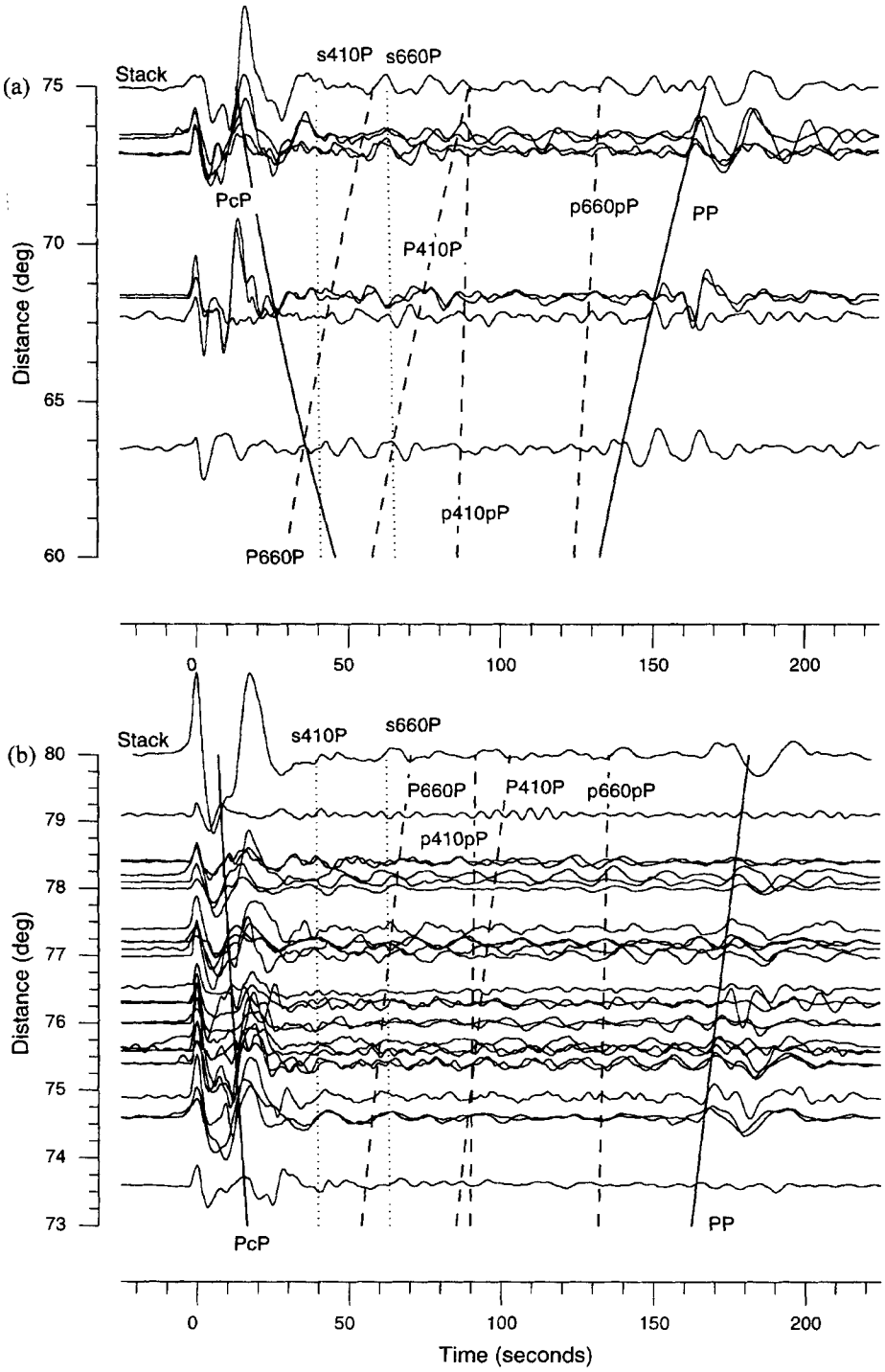


**Figure 5.** (a) Vertical GRF *P*-wave beam WWSSN-LP simulation seismograms for earthquakes between 153°W and 147°W with depths shallower than 80 km. Seismograms are normalized for the interval between 40 and 120 s and aligned on the *P* wave. Top trace is the slant-stack of the seismograms (sum along the traveltime curve *s660P*), where the different event depths are taken into account. Also shown are the predicted arrival times of main (solid lines), converted (dotted) and *P*-multiple (dashed) phases from the IASP91 model for an event at 30 km depth. (b) Same as (a) but for earthquakes between 170°W and 155°W.

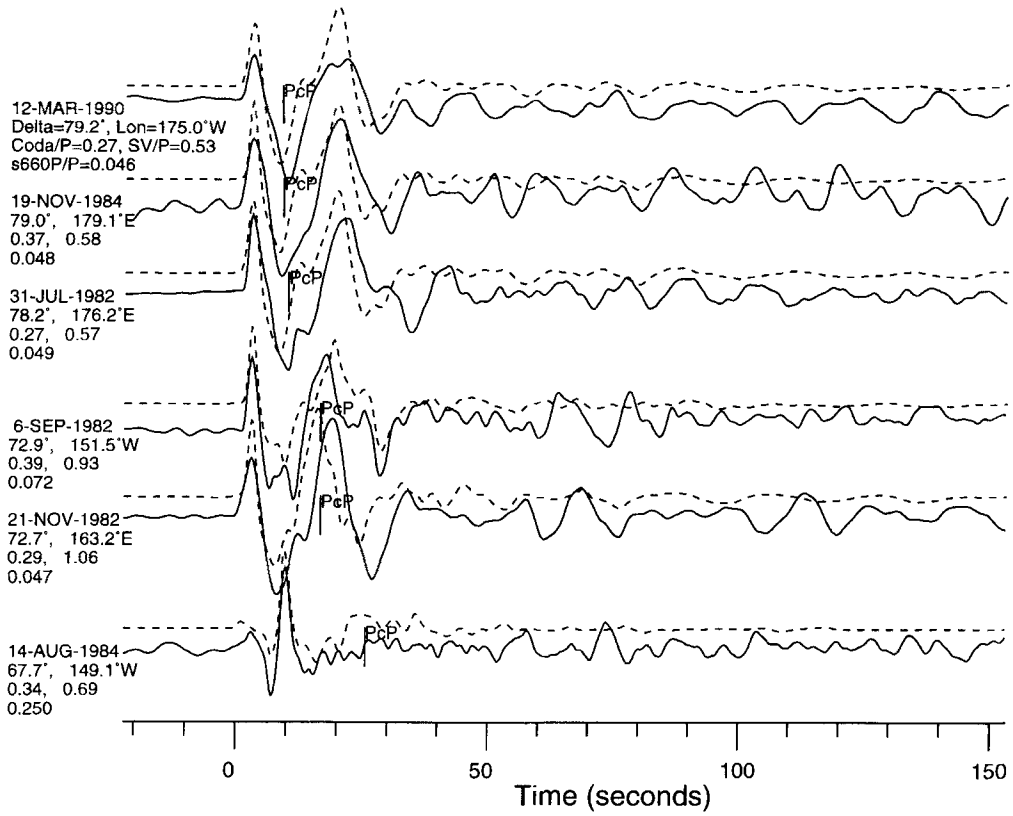


**Figure 6.** Observed (solid line) and theoretical (dashed line) *P*-wave seismograms from selected events. Seismograms have been filtered with the WWSSN-LP filter. Reflectivity seismograms are calculated with the IASP91 model but with appropriate water depth and sediment thickness for each event/receiver combination (Kind 1985); the *PP* wave is not calculated. *Q* and densities are from PREM (Dziewonski & Anderson 1981) and AK135 (Kennett, Engdahl & Buland 1995), respectively. Seismograms are ordered with increasing distance towards the top of the figure. Coda/*P* and *SV*/*P* are the observed ratios (see Fig. 4). *s660P/P* is the theoretical amplitude ratio (Aki & Richards 1980) for the Harvard CMT radiation pattern multiplied by a conversion coefficient of 0.02 for an *SV*-to-*P* conversion at the 660 km discontinuity. 21-NOV-1982 and 6-SEP-1982, at about the same distance from GRF, have similar codas although they are at either end of the Aleutian arc.

The strongest trend in the variation of coda amplitude with longitude along the Aleutian arc is for events in the eastern Gulf of Alaska (east of 145°W), the central Aleutians (180°–170°W) and Kamchatka (155°–165°E) to have substantial energy in the *P*-wave coda, sometimes approaching the amplitude of the *P* wave. To examine a possible dependence of the *P*-coda-to-*P* amplitude ratios on the radiation pattern, we take the ratio of the observed *SV* wave (horizontal) to the *P* wave (vertical) (Fig. 4b) and compare that to the coda-to-*P* ratio (Fig. 4a). In our nomenclature, '*P*' and '*SV*' include the direct and the depth phases. Fig. 4(b) shows a remarkable similarity to Fig. 4(a), suggesting that the *P*-wave coda originates as a phase with an *SV* radiation pattern. In Fig. 4(c) theoretical '*SV*-signal'/'*P*-signal' ratios are calculated for these earthquakes with distances and azimuths to station GRA1. Here, the 'signal' is the maximum of either *S* or *sS*, and of either *P*, *pP* or *sP* calculated from the focal mechanisms of the Harvard centroid moment tensor catalogue. A pattern similar to that in Fig. 4(a) appears, indicating that the coda/signal ratio also has a focal-mechanism dependence.

If the *P*-coda amplitude is a function of the *SV* amplitude, there should be a linear relationship between the two. In Fig. 4(d) *SV*/*P* is plotted against *P* coda/*P* (Fig. 4b versus a): note that while there is large scatter, larger-amplitude *S* waves correlate with large-amplitude *P* codas [e.g. for $SV/P > 1.0$, *P* coda/$P > 0.5$ (or greater than the mean)]. A seismogram from an event at 60.79°N and 167.13°E with $SV/P = 9.37$ and *P* coda/$P = 0.93$ (not plotted due to its extreme values) supports the connection between large *S* and large coda waves. There is, however, a saturation level above which the coda amplitude increases no further. Coda amplitudes should rarely be larger than the *P* wave because converted energy is less than the incident energy. This figure shows that while *SV* energy could be a major factor determining coda amplitudes, it is not the only factor. Deviations from this general trend might be caused by varying orientations of the interface responsible for the *S*-to-*P* conversions and 2-D and 3-D velocity heterogeneities near the epicentres. Slowness analysis (discussed later in the paper) indicates that the coda energy has nearly the same slowness as the *P* wave, meaning that the energy is produced within a few hundred kilometres of the source. Another source of error may be that *S*-wave energy is automatically included in the 'P-wave' amplitude as *sP*. Other candidates, including surface-wave-to-*P* and *P*-to-*P* conversions, will be discussed later in the paper.

Events from the Alaska section of the Aleutian arc (Fig. 2, 147°W to 153°W) appear in Fig. 5(a) as a function of distance from the GRF array (station GRA1). Because waveforms from several nearby events are nearly identical (at 68° and 73° distance in Fig. 5a), an extended source time function (longer than 60 s) can be ruled out as the cause of large coda amplitudes, since for events of differing magnitudes ($m_b$ 5.7–6.3)

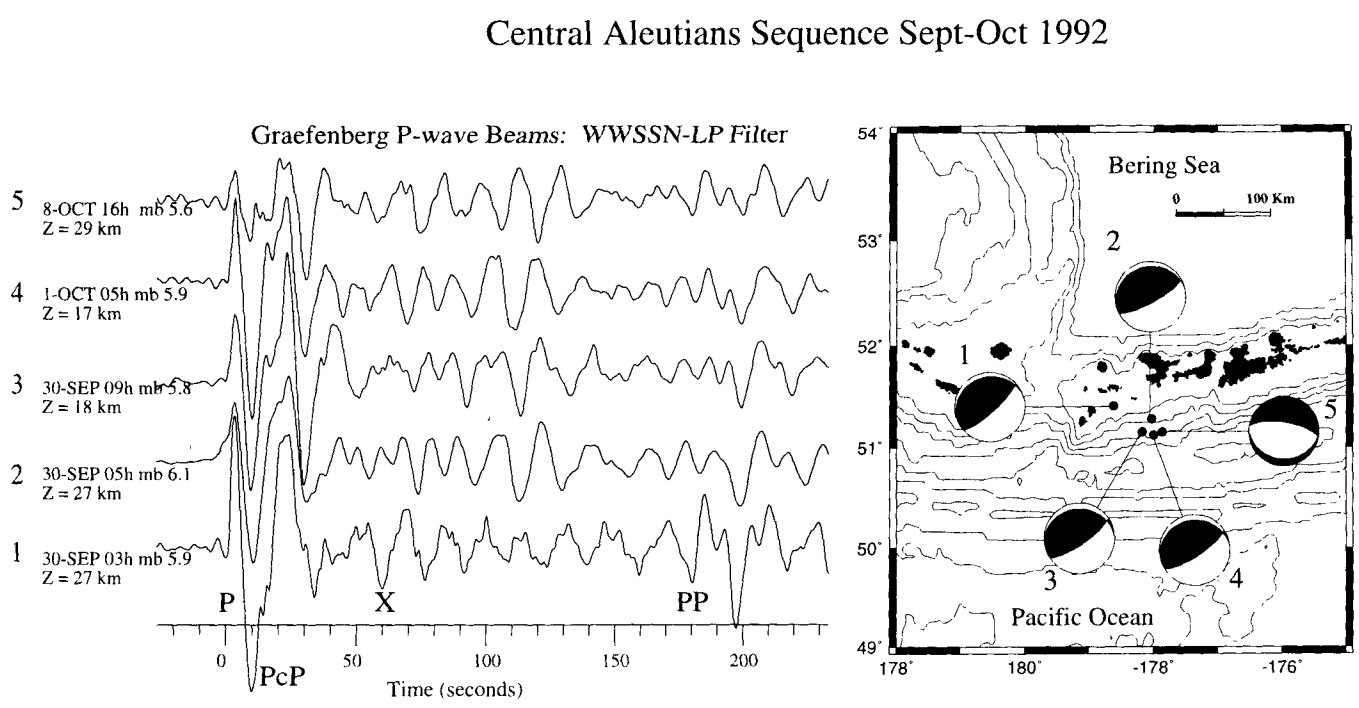


**Figure 7.** Vertical *P*-wave beams from the GRF array filtered with the WWSSN-LP filter. Seismograms are aligned on the maximum amplitude following the first motion. Amplitudes are normalized between 50 and 150 s. Depth ($Z$) is $pP$–$P$ depth from the International Seismological Centre (ISC). Event numbers correspond to those on the location map in the epicentral region shown on the right. Earthquake locations are from PDE and focal mechanisms are from Harvard CMT solutions. The bathymetric contour interval is 1 km; water depth varies from 1 to 3 km. Numbers before the 'h' indicate hour of origin time.

it would indeed be unusual if nearby events had identical source time functions. We perform a similar operation for events in the eastern Aleutians in Fig. 5(b) ($m_b$ 5.7–6.4). Here the *P*-wave codas are relatively quiet as compared with the seismograms in Fig. 5(a).

To explore further the nature of the coda, we enhance the amplitude of the phase at the expected arrival time of *s660P* by slant-stacking the seismograms along the theoretical travel-time curve of *s660P* adjusted for different event depths. Although there is relatively little moveout with distance for *s660P* (as compared with *PcP* and *PP*), the traveltime variation with event depth is about 1 s per 10 km of depth, so there should be considerable moveout with depth for *s410P* and *s660P* (the converted phases arrived closer to *P* for deeper events). The top trace in Fig. 5(b) shows that energy arrives at the expected time of *s660P* with an amplitude of about 10 per cent of the *P* wave. Note that in both Figs 5(a) and (b), the amplitude of *s410P* is smaller than *s660P* (a slant-stack for a conversion at 410 km produced nearly the same result). Uncertainty in event depth, interference from other phases and summation of converted phases of opposite polarity (we make no polarity normalization for the converted phases) may disrupt the slant-stack. Because the phase *s660P* in Fig. 5(b) is only about 10 per cent of the *P* amplitude, we suggest that the phases *s410P* and *s660P* are not the large-amplitude phases in the coda, although they are certainly present in the coda, but with a much smaller amplitude. We will show later that topography on the upper-mantle discontinuities could cause the converted phases *s410P* and *s660P* to have larger amplitudes.

Conversions from the 660 km discontinuity that are larger than those from the 410 km discontinuity are in agreement with other studies. Recently, Vinnik, Kosarev & Petersen (1996) and Kind, Yuan & Estabrook (1997) observed that seismic stations directly over the deeper portions of the subducting Pacific plate report no *S*-to-*P* conversion from the 410 km discontinuity, in contrast to clear observations from the 660 km discontinuity. This observation is in agreement with the slab models of Kirby *et al.* (1996), which have a contorted 410 km discontinuity for old and fast subducting plates; reflections and conversions from a contorted 410 km discontinuity may not be observed. It also supports the model of Pacific slab penetration below 300 km along the Aleutian arc, the depth of the deepest seismicity (Boyd & Creager 1991; Creager & Boyd 1991).

In Fig. 6 we show the results of reflectivity modelling for several events along the Aleutian arc recorded by the GRF array. The initial 30 s of the seismograms are well matched, although the codas between 50 and 80 s are not. Note that the phases in the observed coda are clear and distinct regardless of the theoretical $SV/P$ ratio. Thus, a symmetrically layered earth model cannot explain the amplitudes of the coda phases. The expected amplitudes for thrust events would be about 5 per cent, and those for strike-slip events would be up to 25 per cent.

## CASE STUDY: CENTRAL ALEUTIANS, SEPTEMBER–OCTOBER 1992

Several earthquakes have occurred in the Aleutian/Alaska region since the establishment of the GRSN in 1991. We use these data to augment the GRF data. From September 30 to October 8 1992, six events with $m_b$ 5.6–6.1 occurred in a relatively small area of the central Aleutian arc (Fig. 7).

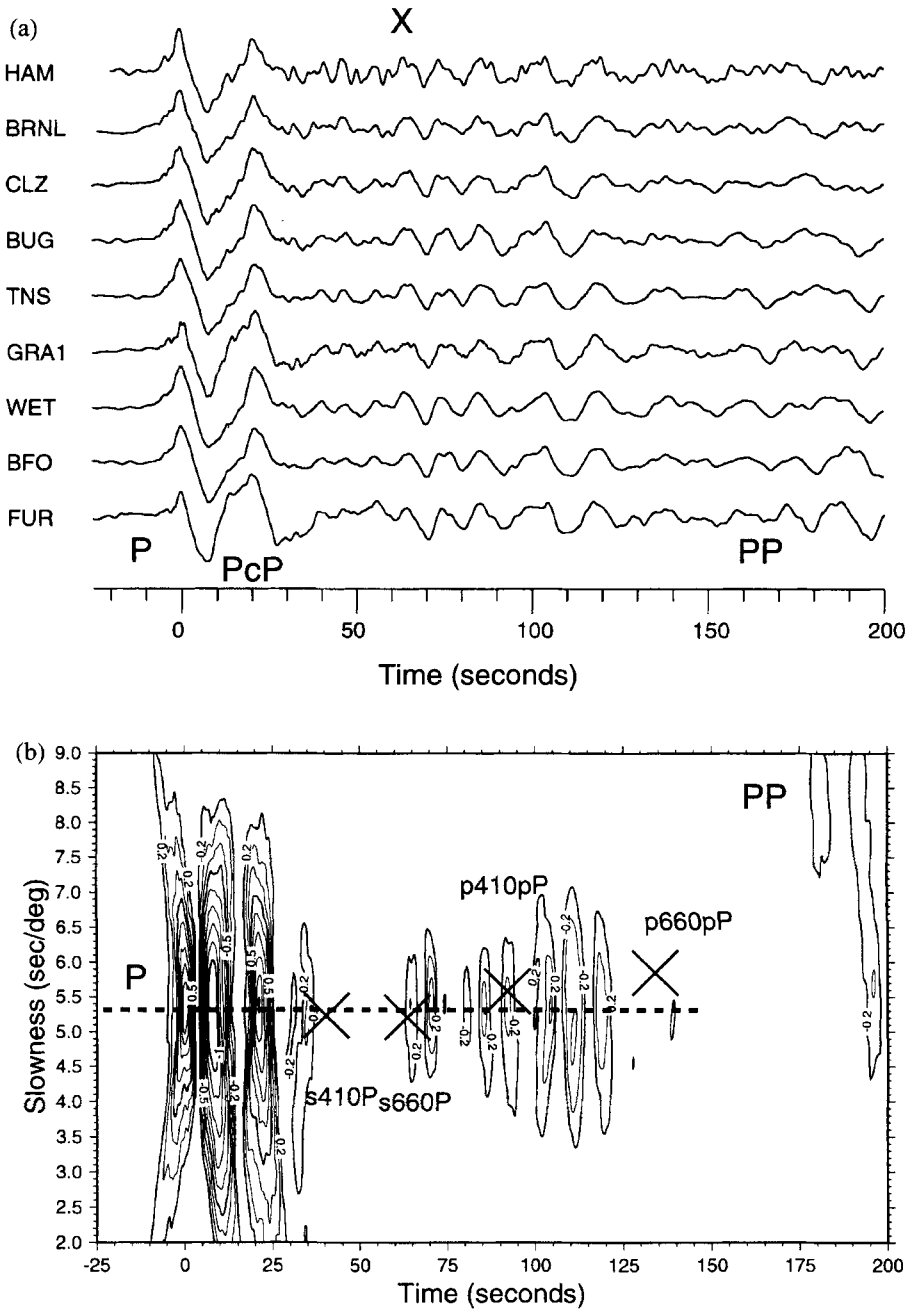


**Figure 8.** (a) GRSN vertical *P*-wave displacement seismograms for event 30-SEP-1992 05 hours (event 2 in Fig. 7). Seismograms have been high-pass filtered at 50 s and ordered with closer stations at the top. Prominent phases are marked. 'X' marks the arrival of large-amplitude coda. (b) Vespagram of seismograms in (a). Contours are linear between 20 per cent and the *P*-wave maximum; data is not contoured below 20 per cent of the maximum. Crosses mark arrivals of labelled phases as calculated from IASP91. (c) GSN seismograms for event in (a). Vertical seismograms are integrated to displacement, normalized and aligned on the *P* wave. Stations closer than 40° are not used. (d) Slowness stack of seismograms in (c) where the data are not contoured below 20 per cent of the maximum. Slowness shift is relative to a *P* wave at 60°. Negative slownesses indicate steeper incidence angles (like *PcP*). Starting at about 50 s, the coda has a slowness slightly smaller than the *P* wave (dashed line).

Waveforms are very similar from event to event for the first 150 s. The seismograms of events 2 and 4 are nearly identical; event 5 is also similar to events 2 and 4, but it has a coda of opposite polarity (note that the mechanism of event 5 is normal faulting while the others are thrust faulting). For events 4 and 5, about 10 km apart horizontally and 12 km in depth, the *P* and *PP* waves have the same polarity but their codas have opposite polarities, implying that either the coda has an entirely different take-off angle or it begins as a wave other than *P*. The plotted epicentres might be in error by several tens of kilometres (Barazangi & Isacks 1979; Fujita, Engdahl & Sleep 1981) because of the presence of the subducting slab, but relative locations are probably accurate because the sets of stations locating the events are nearly the same, and because of the good azimuthal station coverage in 1992. Inhomogeneities between the sources and the GRF array cannot cause the codas of events 4 and 5 to have opposite polarities because the sources are very close together. This effect is wavelength

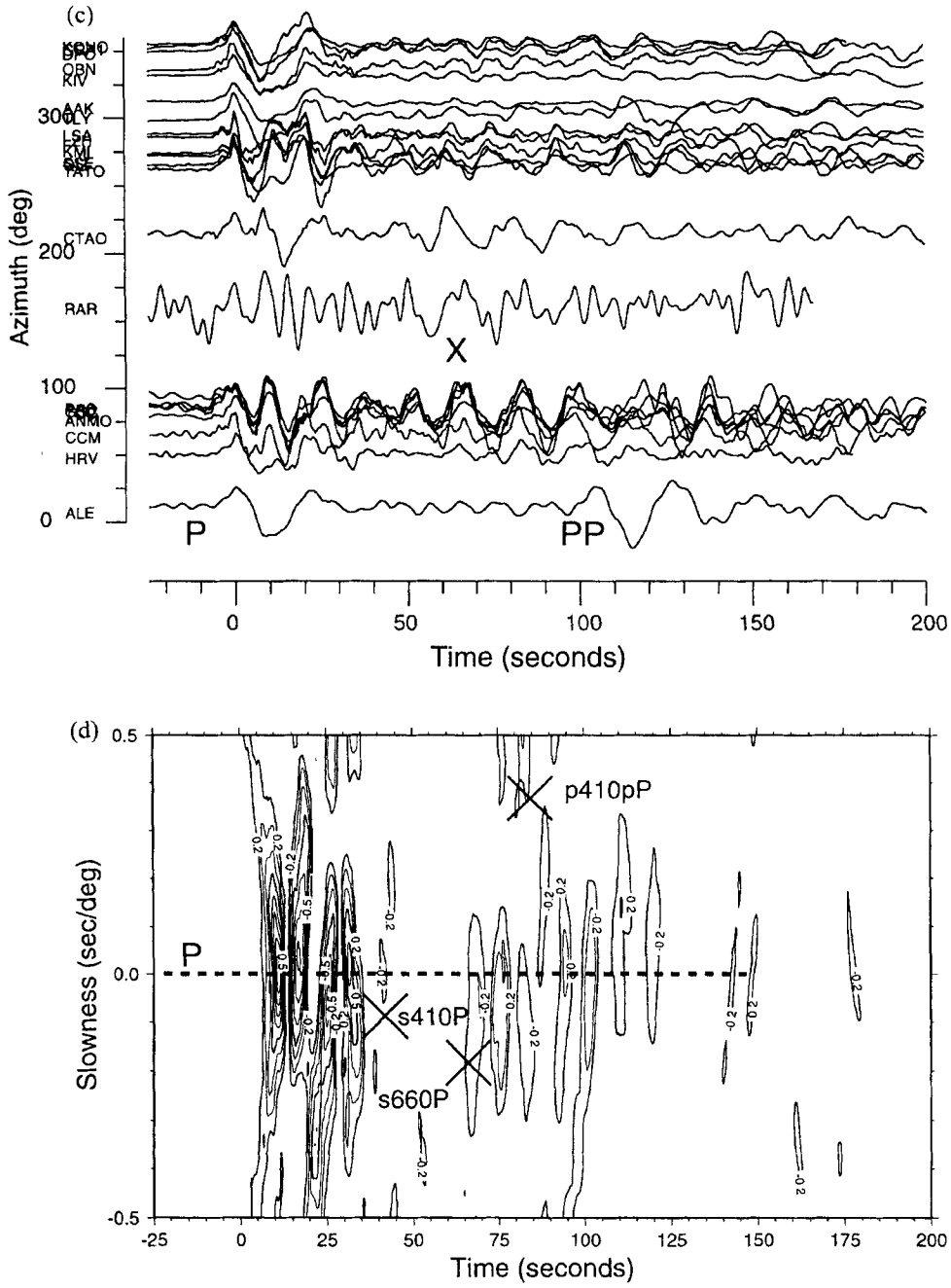


**Figure 8.** *(Continued.)*

($\lambda$) dependent. Seismogram similarity breaks down for events at distances greater than $\lambda/4$ when recorded at the same station (e.g. Aki & Richards 1980, p. 804). For periods of 10–20 s, *P* wavelengths are 60–120 km (assuming a *P*-wave velocity of 6 km $s^{-1}$). The hypocentral distance between these events is about 15 km, slightly smaller than $\lambda/4$. The events can thus be considered to have identical source–receiver paths to GRF; another explanation is needed for their codas of opposite polarity.

We apply array techniques to GRSN seismograms from event 2, the largest event of the swarm, to identify weak phases in the *P*-wave coda from slowness and azimuth information. The GRSN has an aperture of about 7° in distance in the direction of the Aleutian Islands; rays from the Aleutians arrive from the north. Vertical *P*-wave displacement seismograms (Fig. 8a) show a coherent *P* wave of about 30 s duration (including depth phases) and lower-amplitude but coherent coda. To quantify the coherency, we compute a vespagram (slowness as a function of time) (Davies, Kelly & Filson 1971) by time-shifting each seismogram for a given slowness (Fig. 8b). Krüger & Stammler (1996) have shown that a large array such as the GRSN can be used to determine slownesses of seismic waves, provided such measurements are made at long periods. Here the coda waves have about the same slowness as the *P* wave, thus confirming that the coda is originating in the source region.

Broad-band displacement seismograms from globally distributed stations plotted as a function of azimuth (Fig. 8c)

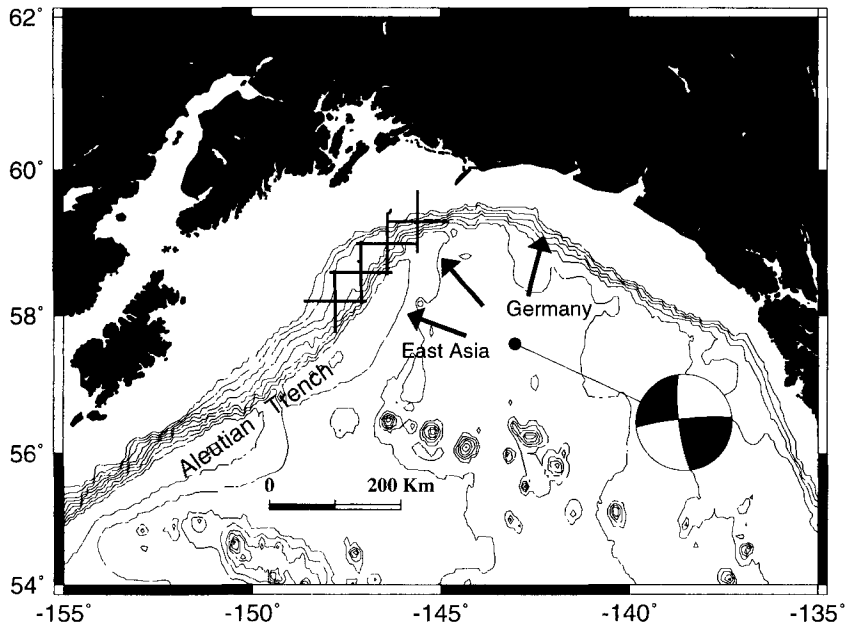


**Figure 9.** Regional map of the Gulf of Alaska showing location of event 7-AUG-1992 (solid circle). Bathymetric contour interval is 500 m. Arrows indicate azimuths of Germany (15°) and East Asia (280°–320°). Focal mechanism shown was determined by body-wave inversion for this study. Crosses near the Aleutian trench indicate a possible *S*-to-*P* conversion region for paths to the East Asian stations.

show a strong coherency for many of the phases between *P* and *PP*. *P*-wave amplitudes vary azimuthally because of the radiation pattern, while the coda does not follow this pattern. At azimuths toward North America (50°–100°), coda waves are coherent and nearly as large as the *P* waves. At CTAO (210°), the coda phase is isolated and nearly as large as the *P* wave. At European azimuths (310°–360°), the *P* waves are much larger relative to the coda waves. The azimuthal variation in coda amplitudes (Fig. 8c) suggests a 3-D influence. Relative amplitudes are largest at azimuths parallel to the Aleutian trench (azimuths 50°–100°) and for paths crossing the trench to the south (RAR and CTAO).

Following the method of Estabrook *et al.* (1994), the GSN seismograms are time-shifted for a given slowness difference relative to the *P* wave and then stacked (Fig. 8d). Relative slowness shifts (compared with absolute shifts in Fig. 8b) are necessary when the distance range is large. Because the only common feature of these seismograms is the source region and uniform global structure, path effects caused by lateral heterogeneity and station structure should be incoherent and cancel out. The slowness analysis indicates that the coda is coherent (with a slowness of 0.1 s/° smaller than the *P* wave) starting about 60 s after the *P* wave. For waves arriving before this time, it is not possible to determine their slownesses because they do not add constructively. The phase arriving at about 65 s has a slowness different from *P* and the arrival time of the converted phase *s660P*. Later arrivals have a larger slowness than *P* (shallower take-off angle) and are consistent with the arrivals of source and receiver side *P* multiples (see Fig. 1).

## CASE STUDY: GULF OF ALASKA, AUGUST 1992

What structures in the source region could contribute to the long-period coda? We consider an event on 1992 August 7 that occurred in the Gulf of Alaska, over 300 km from the coast, in lithosphere having a presumably simple oceanic structure under a nearly constant 3.5–4.0 km layer of water (Fig. 9). Ray tracing with the Gaussian beam method (GBM, e.g. Červený, Popov & Pšenčík 1982; Weber 1988; Davis & Henson 1993) indicates that the bounce points of the water multiples *pwP* and *swP* occur within 10 km of the epicentre. For 3.5 km water depth, *P* waves trapped in the water layer would have a dominant period of about 5 s, would be uniformly distributed in azimuth and have amplitudes considerably smaller that the incident *P* wave (see Ward 1979). However, seismograms from the GSN show that the *P*-wave coda has a strong azimuthal dependence in which stations to the west-northwest (East Asia) have large coda amplitudes compared with the *P* wave. GSN seismograms from this azimuth, shown in Fig. 10a, have codas that are coherent. Note that coda amplitudes are largest for stations whose azimuths are less than 300°, near the minimum in *P* motion (or maximum in *SV* motion for a strike-slip focal mechanism, see below). This is consistent with an *S*-wave origin for the *P* coda. To isolate a source region for this anomalous coda energy, the slowness of the coda of the seismograms (Fig. 10a) is determined. The results (Fig. 10b) show that the coda has a slowness significantly different from the *P* wave (0.1–0.2 s/° greater than *P*). This can be confirmed visually by comparing the moveout of the phase X at MDJ with QIZ.

Seismograms from the GRSN (Fig. 10c) have coda amplitudes approaching that of the *P* wave. We computed a vespagram from these stations, but slownesses were not resolvable, probably because of the longer-period signal (>20 s). This is in contrast to the results from the central Aleutians (Fig. 8a). Here we use the GRSN to constrain the azimuthal variation in the coda. In Fig. 10(d) we calculate beams for varying azimuths at a constant slowness of 5.8 s/°. These results indicate that there is little deviation of the coda energy from the great-circle path (345° from GRA1). The phase at 75 s after *P* has a

maximum azimuth at 347°, about the same azimuth as the conversion region shown in Fig. 9.

To rule out the possibility that an extended source time history could be involved in the creation of the coda, we modelled the event using the method of Nábělek (1984) to determine the focal mechanism, depth and rupture history. The event has a strike-slip mechanism (strike 264°, dip 84°, rake 9°), a depth of 19.5 km, a seismic moment of $1.68 \times 10^{19}$ N m ($M_w$ 6.8) and a duration of 9 s. Using a source time function of significantly longer duration did not improve the fit between observed and synthetic seismograms.

## DISCUSSION

In the following we speculate as to what mechanisms (structural or otherwise) may contribute to large-amplitude *P*-coda waves at teleseismic distances and what causes may be positively ruled out.

### Hypotheses: what the *P* coda is not

Standard phases at this distance range are *PcP*, *PP* and the depth phases *pP* and *sP*. *PcP* and *PP* have slownesses (move-outs) distinct from the observed coda phases. For the distance range 30–80°, the slownesses from the IASP91 velocity model are 8.8–5.4 s/° for *P* waves, 11.1–8.3 s/° for *PP*, and 2.6–4.4 s/° for *PcP*. The observed coda has a slowness close to that of *P*. Double events or extended source processes can be ruled out because adjacent events have similar waveforms despite having magnitudes which vary by one unit of magnitude. Studies of single events show that the amplitudes of the coda phases are azimuth- and frequency-dependent. Similarly, receiver side effects can also be eliminated because of azimuthal similarity as viewed from the source. Source or receiver side *P* multiples from upper-mantle discontinuities arrive too late to have an influence in the first 80 s.

Water and other structural effects in the source region are more difficult to rule out. Ward (1979) examined the effects of water depth and event depth on *P* waves. Ringing *P* waves due to water reverberation are monochromatic starting from the *pP*-wave onset, an effect which is not observed in the Aleutian data set. Engdahl & Kind (1986), however, observed a *P*-wave pulse broadening (not ringing), which they attributed to an effect of the overlying water layer. Wiens (1989) observed, by examining the effects of a dipping seafloor and local structure, that the duration of the amplitude complexities in the *P*-wave coda increase with increasing water depth and seafloor dip. A water depth of about 5 km causes increased amplitudes for the first 50 s of the coda. Okamoto & Miyatake (1989) and Yoshida (1992) considered a 2-D trench model and found that even longer durations could be expected (although only for water depths greater than 5 km, directly above the hypocentres). The events in the central Aleutian sequence (Fig. 7) occur under water depths of 1–3 km, considerably less than that required to cause extended codas. We discount the possibility that water plays a large part in the complexity of these seismograms by examining the event 7-AUG-1992 in the Gulf of Alaska (Fig. 9). The seafloor in this region is nearly flat, thus it is highly unlikely that seafloor bathymetry and structure very close to the source are causing the observed complications in the *P*-wave coda.

An argument against *P*-to-*P* scattering (as is suggested for the coda at local and regional distances) as a primary explanation for the large-amplitude coda waves is that the timing (40 s after the *P* wave) is not consistent with the slowness, which is about the same as the *P* wave. In the case of the Gulf of Alaska event (Figs 9 and 10), the timing of the coda energy would require a *P*-wave scatterer that is nearly double the distance from the source compared to an *S*-wave or surface-wave scatterer (see below). Such a large distance would have a slowness nearly 0.4 s/° larger than that of the *P* wave, something which is not observed.

*PL* (e.g. Shaw & Orcutt 1984; Baag & Langston 1985) can be ruled out because of its large apparent velocity (7–8 km $s^{-1}$) compared to the expected 4 km $s^{-1}$. *Lg*, while having a smaller apparent velocity, has been shown not to propagate in oceanic crust (e.g. Cao & Muirhead 1993; Zhang & Lay 1995; Shapiro *et al.* 1996), a feature necessary for our study. *Sn* (e.g. Stephens & Isacks 1977; Kennett 1985), an *S* wave trapped in a simple layered structure, may travel considerable distances, although the limited thickness of the oceanic lid might filter out the longer periods, and its amplitude would be small (Stephens & Isacks 1977). Simple *S (Sg)* would also have about the correct delay time, but its amplitude would be too small at distances greater than the crustal cross-over distance (about 1°).

### Hypotheses: what it may be

The *P*-wave coda may be composed of waves caused by several mechanisms, and, depending upon conditions unique to a particular region, one mechanism or another may dominate. Studies in the central Aleutians and the Gulf of Alaska suggest that phases in the coda have a different radiation pattern than the *P* wave. Slowness analysis shows that the unusual phases arrive with a slowness about the same as or slightly larger or smaller than the *P* slowness, implying that the coda travels along nearly the same path as the direct *P* wave. A structural feature along the great-circle path between source and receiver close to the source may be causing the phase. The radiation pattern difference suggests an *SV*- or Rayleigh-wave origin. Note that Rayleigh waves involve interacting *P*–*SV* at the free surface. For most of the Aleutians we cannot distinguish between a Rayleigh- and an *SV*-wave origin. Only for the earthquake in the Gulf of Alaska do we have enough information to distinguish between the two.

In the case of the Gulf of Alaska earthquake, we suggest that Rayleigh waves propagating in the oceanic crust convert to *P* waves when they encounter the dipping Aleutian plate. This is in support of the observation that tectonic features like subduction zones can act as very efficient reflectors of seismic waves (Wright & Muirhead 1969; Husebye & Madariaga 1970; Weber & Wicks 1996; Wicks *et al.* 1997). Other events in the Gulf of Alaska (Fig. 2) also have large codas, but they occurred before 1990, thus limiting the analyses of these events to GRF data only. Fig. 10(b) shows that coda energy arrives between 50 and 75 s after and at 0.1–0.2 s/° greater than the *P* wave. If we confine conversions to the great-circle path, 0.1–0.2 s/° corresponds to a path which is 100–200 km closer to the stations. A wave travelling at 3–4 km $s^{-1}$ for 200 km, then converting to a *P* wave satisfies these conditions. Waves which originate as an *SV* or Rayleigh wave, both of which have phase velocities of 3–4 km $s^{-1}$, would satisfy the observed delay-time requirement. We favour a Rayleigh-wave origin because the

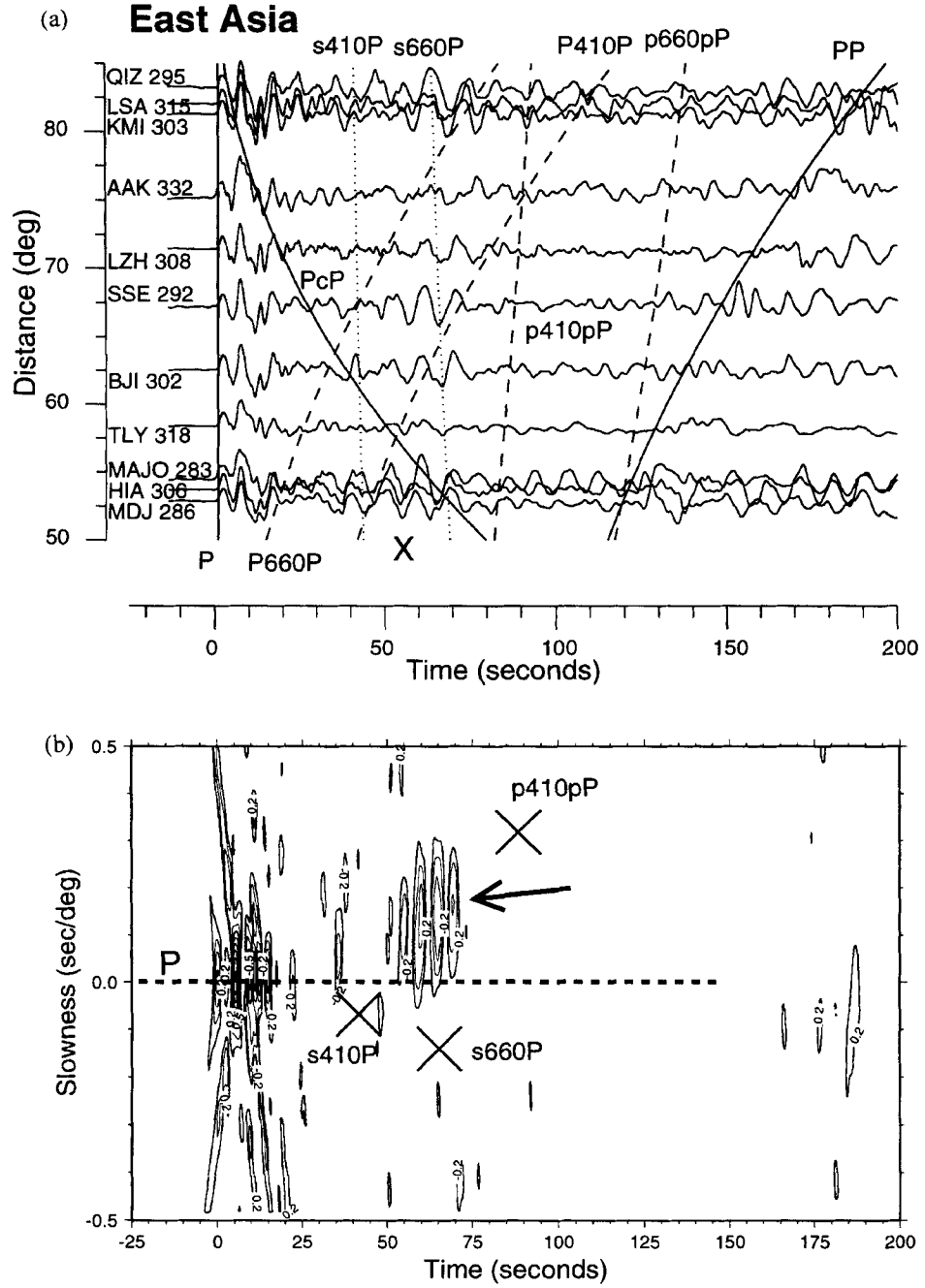


**Figure 10.** (a) GSN seismograms for event 7-AUG-1992 for azimuths between 280° and 330°. Vertical seismograms are integrated to displacement, normalized and aligned on the *P* wave. Also shown are the predicted arrival times of main (solid lines), converted (dotted lines) and *P*-multiple (dashed lines) phases from the IASP91 model. 'X' marks the large-amplitude phase in the coda. Number next to station code is the azimuth from the epicentre. (b) Slowness stack of seismograms in (a). Slowness shift is relative to the slowness of a *P* wave at 70°. Negative slownesses indicate steeper incidence angles (like *PcP*). Starting at about 50 s after the *P* wave, the coda has a slowness 0.1–0.2 s/° larger than the *P* wave (arrow). (c) Seismograms for the GRSN. (d) Azimuthal stack of seismograms in (c) showing azimuthal dependence of the coda. The backazimuth of the beam was calculated in 1° steps for a constant slowness of 5.8 s/°. There is a slight tendency for the coda (75 s) to have a larger backazimuth (347°) compared with the initial *P* wave (345°), which is consistent with an *S*-to-*P* conversion location shown in (a).

amplitudes of *SV* waves (*Sn* or *Sg*) would be too small at a distance of 2°.

When the layered structure suddenly ends, there could be considerable seismic radiation emanating some distance from the source as a secondary Huygens source. The correlation of high coda amplitude with oceanic crust suggests that a simple layered crustal structure is conducive to amplification and propagation of *P–SV* waves. Continental crust may be too thick and heterogeneous to support internal reflections in the period range of body waves.

*P*-to-Rayleigh conversions have been considered as a likely cause of extended *P*-wave codas from stations that occur over sedimentary basins (e.g. Kawase & Aki 1989); such conversions would occur near the station. Reciprocity implies that

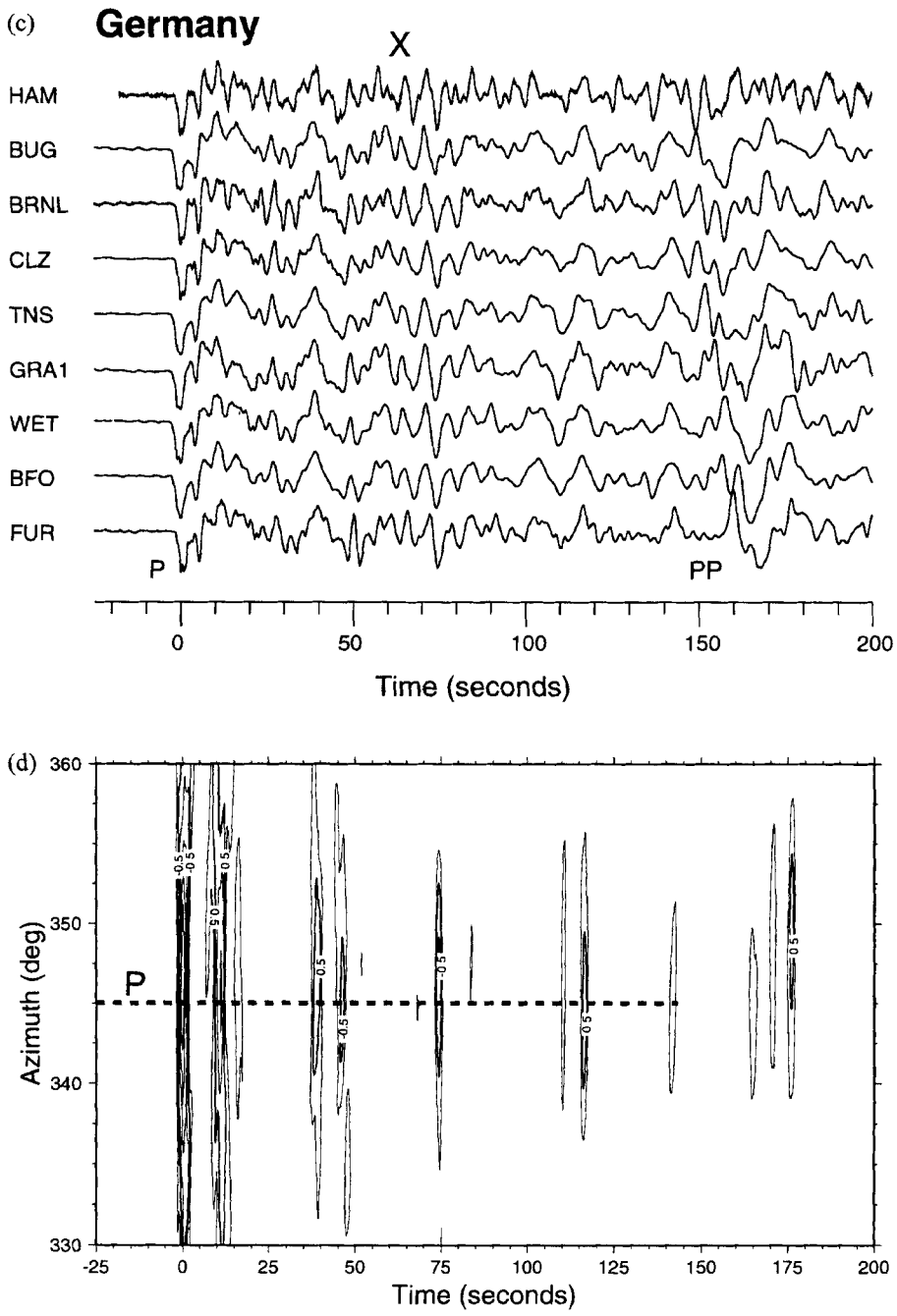


**Figure 10.** (*Continued.*)

Rayleigh-to-*P* conversions near the source might also be significant, and they have been shown to contribute to the teleseismic *P*-wave coda (e.g. Greenfield 1971; Springer 1974; Lynnes & Lay 1989; Nakanishi 1992; McLaughlin *et al.* 1992; Krüger *et al.* 1996). A Rayleigh wave propagating only a few cycles (several hundred kilometres) disperses little, and might retain a pulse-like character and thus be consistent with the observations. It loses little of its initial amplitude through geometrical spreading, so that considerable energy would remain to radiate as a *P* wave from a secondary source.

We now explore what type of *SV* wave might be involved in the coda generation. *S*-to-*P* conversions from upper-mantle seismic discontinuities have slownesses slightly smaller than the *P* wave, consistent with the observations from the central Aleutian events (Fig. 8). Problems with this hypothesis are in the amplitudes of the converted phases and the lack of significant depth dependence. Topography on the 410 and 660 km discontinuities may play an important role in determining the amplitudes of the *S*-to-*P* conversions at these discontinuities by focusing the rays from the conversions as observed at teleseismic distances. To this end, we model topography by altering the depth of the 410 and 660 km discontinuities in the IASP91 velocity model and tracing rays through the model using the GBM (Fig. 11a). The discontinuities are adjusted 50 km upwards (410) and downwards (660) over 1000 km laterally, in accordance with what is expected from the

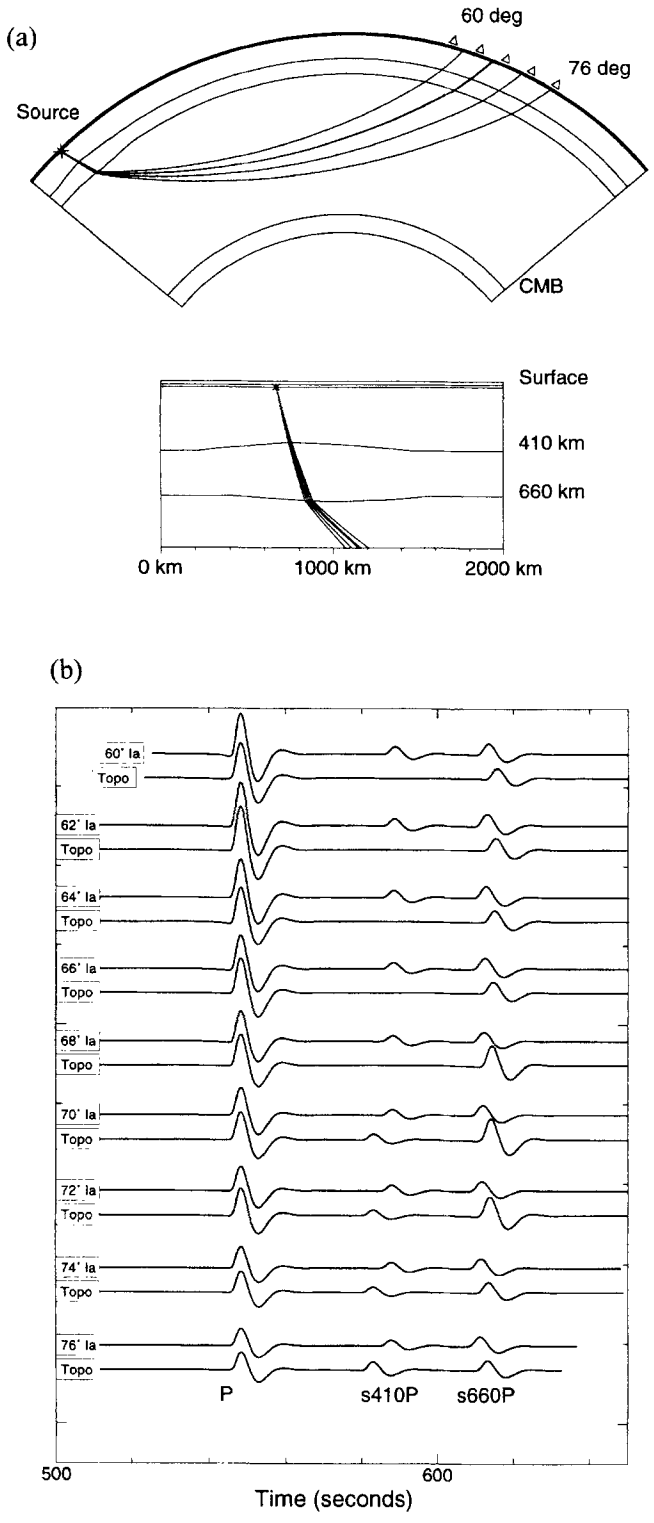


**Figure 11.** (a) Ray diagram showing rays traced through the modified IASP91 velocity model with discontinuity topography. Rays start as *S*-waves and are then converted to *P* waves at the 660 km discontinuity. The rectangle shows an enlargement of the conversion region. CMB is the core–mantle boundary. (b) Seismograms calculated for the IASP91 model (Ia) and for the topography model (Topo) in (a) using the GBM. Seismograms are ordered by epicentral distance. We use a focal mechanism of strike 117°, dip 14°, slip −157°, station azimuth 170° and earthquake depth 37 km, which produces strong *SV* radiation. The source function is a two-sided Küpper wavelet with a duration of 3 s, *Q* is from PREM and density is from AK135. Note that *s410P* and *s660P* vary smoothly with distance. The upward curvature of the 410 km discontinuity causes defocusing between 60° and 68°; downward curvature of the 660 km causes focusing between 68° and 72°. The exact position of the focusing–defocusing depends on the source location with respect to the anomaly.

interaction of a cold subducting slab with the mantle transition zone (e.g. Revenaugh & Jordan 1991; Christensen 1996), although the amplitudes of the topography might be extreme.

The effect of this topography on conversions from the 410 km discontinuity is to cause defocusing of rays at teleseismic distances. Downward deflection of the 660 km discontinuity causes focusing of rays in the teleseismic range. The ray diagram shows that the angle of the interface, not the absolute topography, determines the ray path; narrow anomalies would have an extreme effect on the wavefield at teleseismic distances. For more detailed models of focusing and defraction of energy by subduction zones, see Weber (1990). Using this altered earth model, we calculate synthetic seismograms (Fig. 11b) using the GBM. The effect of the focusing is to double the amplitude of the *s660P* phases compared to the standard model between 68° and 72°. Defocusing of *s410P* causes the phase to almost disappear at distances less than 68°. These results agree with those of van der Lee, Paulssen & Nolet (1994), who showed that large *S* conversions from the 660 km discontinuity under the receiver (*P660s*) can be explained by topography of 15–25 km over several hundreds of kilometres.

## CONCLUSIONS

We have investigated large-amplitude phases arriving in the *P*-wave coda of broad-band seismograms from teleseisms recorded by the Gräfenberg array, the GRSN and the GSN. Theoretical modelling indicated that phases in the *P*-wave coda cannot be *P*-wave multiples beneath the source and receiver, and underside reflections from upper-mantle discontinuities that precede *PP*, because their slownesses and/or amplitudes do not fit our observations. Our study of Aleutian earthquakes indicated that the *P* coda has a different radiation pattern to the *P* wave and is possibly of *SV* origin. Large-amplitude coda waves correlate with the presence of oceanic crust in the source region. *S*-to-*P*-wave conversions from upper-mantle discontinuities may account for the large-amplitude phases in the *P*-wave coda, but only if the amplitudes are enhanced by discontinuity topography. Because there is little, if any, dependence on event depth for the large amplitude coda, we suggest that the large-amplitude phases in the *P*-wave coda originate as *SV* waves and are enhanced by lateral heterogeneity and multipathing/waveguide effects from the subducting Aleutian slab. An alternative explanation is a near-source Rayleigh-to-*P* conversion.

## ACKNOWLEDGMENTS

We thank Günter Bock, Klaus Stammler and Jürgen Gossler for helpful discussions. Günter Bock, Michael Korn, Frank Krüger, Gerhard Müller and Hanneke Paulssen provided thoughtful reviews of the manuscript. Klaus Stammler helped to access the GRF data, and the staff at IRIS-Seattle, Winfried Hanka and Willi Rüsing, helped with the GSN and GRSN

data. We made use of the GMT software (Wessel & Smith 1991) in creating some of the figures. This research was supported by the Deutsche Forschungsgemeinschaft.

## REFERENCES


Aki, K. & Chouet, B., 1975. Origin of coda waves: Source attenuation and scattering effects, *J. geophys. Res.*, **80,** 3322–3342.

Aki, K. & Richards, P., 1980. *Quantitative Seismology, Theory and Methods,* Vols. 1 & 2, W.H. Freeman & Co., San Francisco, CA.

Baag, C.-E. & Langston, C.A., 1985. Shear-coupled *PL, Geophys. J. R. astr. Soc.*, **80,** 363–386.

Barazangi, M. & Isacks, B.L., 1979. A comparison of the spatial distribution of mantle earthquakes determined from data produced by local and by teleseismic networks for the Japan and Aleutian arcs, *Bull. seism. Soc. Am.*, **69,** 1763–1770.

Barley, B.J., Hudson, J.A. & Douglas, A., 1982. *S* to *P* scattering at the 650 km discontinuity, *Geophys. J. R. astr. Soc.*, **69,** 159–172.

Bock, G. & Ha, J., 1984. Short-period *S-P* conversion in the mantle at a depth near 700 km, *Geophys. J. R. astr. Soc.*, **77,** 593–615.

Bock, G. & Kind, R., 1991. A global study of *S*-to-*P* and *P*-to-*S* conversions from the upper mantle transition zone, *Geophys. J. Int.*, **107,** 117–129.

Bolt, B.A., O'Neill, M. & Qamar, A., 1968. Seismic waves near 110°: is structure in core or upper mantle responsible?, *Geophys. J. R. astr. Soc.*, **16,** 475–487.

Boyd, T.M. & Creager, K.C., 1991. The geometry of Aleutian subduction: Three-dimensional seismic imaging, *J. geophys. Res.*, **96,** 2267–2291.

Cao, S. & Muirhead, K.J., 1993. Finite difference modelling of *Lg* blockage, *Geophys. J. Int.*, **115,** 85–96.

Cleary, J. R., King, D.W. & Haddon, R.A.W., 1975. *P*-wave scattering in the Earth's crust and upper mantle, *Geophys. J. R. astr. Soc.*, **43,** 861–872.

Červený, V., Popov, M.M. & Pšenčík, I., 1982. Computation of wave fields in inhomogeneous media—Gaussian beam approach, *Geophys. J. R. astr. Soc.*, **70,** 109–128.

Christensen, U.R., 1996. The influence of trench migration on slab penetration into the lower mantle, *Earth planet. Sci. Lett.*, **140,** 27–39.

Creager, K.C. & Boyd, T.M., 1991. The geometry of Aleutian subduction: Three-dimensional kinematic flow model, *J. geophys. Res.*, **96,** 2293–2307.

Dainty, A.M. & Schultz, C.A., 1995. Crustal reflections and the nature of regional *P*-coda, *Bull. seism. Soc. Am.*, **85,** 851–858.

Davies, D., Kelly, E.J. & Filson, J. R., 1971. Vespa process for analysis of seismic signals, *Nature, Phys. Sci.*, **232,** 8.

Davies, J., Sykes, L., House, L. & Jacob, K., 1981. Shumagin seismic gap, Alaska Peninsula: History of great earthquakes, tectonic setting and evidence for high seismic potential, *J. geophys. Res.*, **86,** 3821–3855.

Davis, J.P. & Henson, I.H., 1993. *User's Guide to Xgbm: An X-windows System to Compute Gaussian Beam Synthetic Seismograms,* TGAL-93-02, Phillips Laboratory, Hanscom AFB, MA.

Dziewonski, A.M. & Anderson, D.L., 1981. Preliminary reference Earth model, *Phys. Earth planet. Inter.*, **25,** 297–356.

Engdahl, E.R. & Kind, R., 1986. Interpretation of broad-band seismograms from central Aleutian earthquakes, *Ann. Geophys.*, **4,** 233–240.

Estabrook, C.H. & Jacob, K.H., 1991. Stress indicators in Alaska, in *Neotectonics of North America,* eds Slemmons, D.B., Engdahl, E.R., Zoback, M.D. & Blackwell, D.D., *Decade Map,* **1,** 387–399, Geol. Soc. Am., Boulder, CO.

Estabrook, C.H. & Kind, R., 1996. The nature of the 660-kilometer upper mantle seismic discontinuity from precursors to the PP phase, *Science,* **274,** 1179–1182.

Estabrook, C.H., Bock, G. & Kind, R., 1994. Investigation of mantle discontinuities from a single deep earthquake, *Geophys. Res. Lett.*, **21,** 1495–1498.

Faber, S. & Müller, G., 1980. *Sp* phases from the transition zone between the upper and lower mantle, *Bull. seism. Soc. Am.*, **70,** 487–508.

Fujita, K., Engdahl, E.R. & Sleep, N.H., 1981. Subduction zone calibration and teleseismic relocation of thrust zone events in the central Aleutian islands, *Bull. seism. Soc. Am.*, **71,** 1805–1828.

Greenfield, R.J., 1971. Short-period *P*-wave generation by Rayleigh-wave scattering at Novaya Zemlya, *J. geophys. Res.*, **76,** 7988–8002.

Harjes, H.-P. & Seidl, D., 1978. Digital recording and analysis of broadband seismic data of the Graefenberg (GRF) Array, *J. Geophys.*, **44,** 511–523.

Helffrich, G. & Stein, S., 1993. Study of the structure of the slab–mantle interface using reflected and converted seismic waves, *Geophys. J. Int.*, **115,** 14–40.

Hori, S., Inoue, H., Fukao, Y. & Ukawa, M., 1985. Seismic detection of the untransformed 'basaltic' oceanic crust subducting into the mantle, *Geophys. J. R. astr. Soc.*, **83,** 169–197.

Husebye, E. & Madariaga, R., 1970. The origin of precursors to core waves, *Bull. seism. Soc. Am.*, **60,** 939–952.

Jacob, K.H., Nakamura, K. & Davies, J.N., 1977. Trench-volcano gap along the Alaska-Aleutian Arc: Facts, and speculations on the role of terrigenous sediments for subduction, in *Island Arcs, Deep Sea Trenches and Back Arc Basins,* Ewing Vol. 1, pp. 243–258, eds Talwani, M. & Pitman, W., Am. Geophys. Un.

Kawase, H. & Aki, K., 1989. A study on the response of a soft basin for incident *S, P,* and Rayleigh waves with special reference to the long duration observed in Mexico City, *Bull. seism. Soc. Am.*, **79,** 1361–1382.

Kennett, B.L.N., 1985. On regional S, *Bull. seism. Soc. Am.*, **75,** 1077–1086.

Kennett, B.L.N. & Engdahl, E.R., 1991. Traveltimes for global earthquake location and phase identification, *Geophys. J. Int.*, **105,** 429–465.

Kennett, B.L.N., Engdahl, E.R. & Buland, R., 1995. Constraints on seismic velocities in the Earth from traveltimes, *Geophys. J. Int.*, **122,** 108–124.

Kind, R., 1979. Extensions of the reflectivity method, *J. Geophys.*, **45,** 373–380.

Kind, R., 1985. The reflectivity method for different source and receiver structures and comparison with GRF data, *J. Geophys.*, **58,** 146–152.

Kind, R. & Seidl, D., 1982. Analysis of broadband seismograms from the Chile-Peru area, *Bull. seism. Soc. Am.*, **72,** 2131–2145.

Kind, R. & Seidl, D., 1984. Reply to A. Douglas, R.C. Stewart & L. Richardson's 'Comments on "Analysis of broadband seismograms from the Chile-Peru area"', *Bull. seism. Soc. Am.*, **74,** 779–780.

Kind, R. & Seidl, D., 1986. Reply to I.G. Stimpson's 'Comment on "Analysis of broadband seismograms from the Chile-Peru area"', *Bull. seism. Soc. Am.*, **76,** 1157–1160.

Kind, R., Yuan, X. & Estabrook, C.H., 1997. Effects of the subducting Pacific plate on the upper-mantle seismic discontinuities, *Science,* submitted.

King, D.W., Haddon, R.A.W. & Husebye, E.S., 1975. Precursors to *PP, Phys. Earth planet. Inter.*, **10,** 103–127.

Kirby, S.H., Stein, S., Okal, E.A. & Rubie, D.C., 1996. Metastable mantle phase transformations and deep earthquakes in subducting oceanic lithosphere, *Rev. Geophys.*, **34,** 261–306.

Klemperer, S.L., Galloway, B., Childs, J. R. & Bering-Chukchi Working Group, 1995. Preliminary results of deep seismic profiling offshore Alaska from the Aleutian basin to the Arctic ocean, *EOS, Trans. Am. geophys. Un., supplement,* **76** (46), 590 (abstract).

Krüger, F. & Stammler, K., 1996. The German Regional Seismic Network (GRSN) used as mid- and longperiod array (abstract), *Ann. Geophys.*, **14,** C44.

Krüger, F., Scherbaum, F., Weber, M. & Schlittenhardt, J., 1996. Analysis of asymmetric multipathing with a generalization of the double beam method, *Bull. seism. Soc. Am.*, **86,** 737–749.

Lay, T., 1987. Analysis of near-source contributions to early *P*-wave coda for underground explosions. III. Inversions for isotropic scatterers, *Bull. seism. Soc. Am.*, **77,** 1767–1783.

Lu, Z. & Wyss, M., 1996. Segmentation of the Aleutian plate boundary derived from stress direction estimates based on fault plane solutions, *J. geophys. Res.*, **101,** 803–816.

Lynnes, C.S. & Lay, T., 1989. Inversion of *P* coda for isotropic scatterers at the Yucca Flat test site, *Bull. seism. Soc. Am.*, **79,** 790–804.

McLaughlin, K.L., Barker, T.G., Day, S.M., Shkoller, B. & Stevens, J.L., 1992. Effects of subduction zone structure on explosion-generated Rayleigh waves: 3-D numerical simulations, *Geophys. J. Int.*, **111,** 291–308.

Nábělek, J.L., 1984. Determination of earthquake source parameters from inversion of body waves, *PhD thesis,* Massachusetts Institute of Technology, Cambridge, MA.

Nakanishi, I., 1980. Precursors to *ScS* phases and dipping interface in the upper mantle beneath southwestern Japan, *Tectonophysics,* **69,** 1–35.

Nakanishi, I., 1992. Rayleigh waves guided by sea-trench topography, *Geophys. Res. Lett.*, **12,** 2385–2388.

Neele, F. & Snieder, R., 1991. Are long-period body wave coda caused by lateral heterogeneity? *Geophys. J. Int.*, **107,** 131–153.

Okamoto, T. & Miyatake, T., 1989. Effects of near source seafloor topography on long-period teleseismic *P* waveforms, *Geophys. Res. Lett.*, **16,** 1309–1312.

Revenaugh, J. & Jordan, T.H., 1991. Mantle layering from *ScS* reverberations 2. The transition zone, *J. geophys. Res.*, **96,** 19 763–19 780.

Richards, M.A. & Wicks, C.W., 1990. *S–P* conversion from the transition zone beneath Tonga and the nature of the 670 km discontinuity, *Geophys. J. Int.*, **101,** 1–35.

Ritsema, J., Hagerty, M. & Lay, T., 1995. Comparison of broadband and short-period seismic waveform stacks: Implications for upper-mantle discontinuity structure, *Geophys. Res. Lett.*, **22,** 3151–3154.

Sato, H., 1994. Multiple isotropic scattering model including *P–S* conversions for the seismogram envelope formation, *Geophys. J. Int.*, **117,** 487–494.

Shapiro, N., Bethoux, N., Campillo, M. & Paul, A., 1996. Regional seismic phases across the Ligurian Sea: *Lg* blockage and oceanic propagation, *Phys. Earth planet. Int.*, **93,** 257–268.

Shaw, P. & Orcutt, J., 1984. Propagation of *PL* and implications for the structure of Tibet, *J. geophys. Res.*, **89,** 3135–3152.

Shearer, P.M., 1991. Constraints of upper mantle discontinuities from observations of long-period reflected and converted phases, *J. geophys. Res.*, **96,** 18 147–18 182.

Springer, D.L., 1974. Secondary sources of seismic waves from underground nuclear explosions, *Bull. seism. Soc. Am.*, **64,** 581–594.

Stammler, K., 1992. Ein Beitrag zur Untersuchung des oberen Erdmantels mit Hilfe von *PS*-Konversionsphasen, *Dissertation,* Universität Nürnberg.

Stammler, K., 1993. SeismicHandler—programmable multichannel data handler for interactive and automatic processing of seismological analyses, *Comput. Geosci.*, **19,** 135–140.

Stephens, C. & Isacks, B.L., 1977. Toward an understanding of *Sn*: Normal modes of Love waves in an oceanic structure, *Bull. seism. Soc. Am.*, **67,** 69–78.

Taber, J.J., Billington, S. & Engdahl, E.R., 1991. Seismicity of the Aleutian Arc, in *Neotectonics of North America,* eds Slemmons, D.B., Engdahl, E.R., Zoback, M.D. & Blackwell, D.D., *Decade Map,* **1,** 29–46, Geol. Soc. Am., Boulder, CO.

van der Lee, S., Paulssen, H. & Nolet, G., 1994. Variability of P660s phases as a consequence of topography of the 660 km discontinuity, *Phys. Earth planet. Inter.*, **86,** 147–164.

Vidale, J.E. & Benz, H.M., 1992. Upper-mantle seismic discontinuities and the thermal structure of subduction zones, *Nature,* **356,** 678–683.

Vinnik, L., Kosarev, G. & Petersen, N., 1996. Mantle transition zone beneath Eurasia, *Geophys. Res. Lett.*, **23,** 1485–1488.

Ward, S.N., 1978. Long-period reflected and converted upper-mantle phases, *Bull. seism. Soc. Am.*, **68,** 133–153.

Ward, S.N., 1979. Ringing *P* waves and submarine faulting, *J. geophys. Res.*, **84,** 3057–3062.

Weber, M., 1988. Computation of body-wave seismograms in absorl ing 2-D media using the Gaussian beam method: Comparison wit exact methods, *Geophys. J.*, **92,** 9–24.

Weber, M., 1990., Subduction zones—their influence on traveltimes and amplitudes of *P*-waves, *Geophys. J. Int.*, **101,** 529–544.

Weber, M. & Wicks, C.W., 1996. Reflections from a distant subduction zone, *Geophys. Res. Lett.*, **23,** 1453–1456.

Wessel, P. & Smith, W.H.F., 1991. Free software helps map and display data, *EOS, Trans. Am. geophys. Un.*, **72,** 441, 445–446.

Wicks, C.W. & Richards, M.A., 1991. Effects of source radiation patterns on the phase $S_{670}P$ beneath the Tonga subduction zone, *Geophys. J. Int.*, **107,** 279–290.

Wicks, C.W., Weber, M., LeStunff, Y. & Romanowicz, B., 1997. Seismic evidence for a fossil slab in the mantle transition zone near the west Mariana arc, *Nature,* submitted.

Wiens, D.A., 1989. Bathymetric effects on body waveforms from shallow subduction zone earthquakes and application to seismic processes in the Kurile trench, *J. geophys. Res.*, **94,** 2955–2972.

Wright, C., 1972. Array studies of seismic waves arriving between *P* and *PP* in the distance range 90° to 115°, *Bull. seism. Soc. Am.*, **62,** 385–400.

Wright, C. & Muirhead, K.J., 1969. Longitudinal waves from the Novaya Zemlya nuclear explosion of October 27, 1966, recorded at the Warramunga seismic array, *J. geophys. Res.*, **74,** 2034–2048.

Yoshida, S., 1992. Waveform inversion for rupture process using a non-flat seafloor model: Application to 1986 Andreanof Islands and 1985 Chile earthquakes, *Tectonophysics,* **211,** 45–59.

Zhang, T.-R. & Lay, T., 1995. Why the *Lg* phase does not traverse oceanic crust, *Bull. seism. Soc. Am.*, **85,** 1665–1678.